J Low Temp Phys (2011) 163: 317–344
DOI 10.1007/s10909-011-0353-1

# Acoustic Emission by Quartz Tuning Forks and Other Oscillating Structures in Cryogenic $^4$He Fluids

**D. Schmoranzer · M. La Mantia · G. Sheshin ·
I. Gritsenko · A. Zadorozhko · M. Rotter ·
L. Skrbek**

Received: 7 December 2010 / Accepted: 17 February 2011 / Published online: 4 March 2011

**Abstract** We report on experimental investigations of acoustic emission by quartz tuning forks resonating at frequencies 32 kHz, 38 kHz, 77 kHz and 100 kHz immersed in cold gaseous $^4$He and its normal and superfluid liquid phases. Frequency dependence of the observed low-drive-linewidth at 350 mK together with the temperature and pressure dependences ($1.3\ \mathrm{K} < T < 4.2\ \mathrm{K}$, $0 < p < 25$ bar) of the observed damping of the high frequency (77 and 100 kHz) resonators measured in normal liquid $^4$He and its superfluid phase provide strong and direct evidence of the importance of sound emission by these tuning forks. Three analytical models of acoustic emission by vibrating tuning forks are developed and compared with the experimental results. We also discuss the importance of sound emission for experiments with the commonly used 32 kHz tuning forks as well as other oscillating structures—spheres, wires, grids and various micromachined sensors. We compare the relative importance of dissipative losses due to laminar viscous/ballistic drag and acoustic emission in liquid and superfluid $^4$He.

**Keywords** Quartz tuning fork · Cryogenic helium · Acoustic emission

## 1 Introduction

Quartz tuning forks, mass produced as frequency standards for digital watches with a large number of other applications [1, 2], have recently become popular research

---

D. Schmoranzer (✉) · M. La Mantia · M. Rotter · L. Skrbek
Faculty of Mathematics and Physics, Charles University, V Holesovickach 2, 180 00, Prague, Czech Republic
e-mail: david.schmoranzer@mff.cuni.cz

G. Sheshin · I. Gritsenko · A. Zadorozhko
B. Verkin Institute for Low Temperature Physics and Engineering, 47 Lenin Ave., 61103, Kharkov, Ukraine

tools in cryogenic fluid dynamics [3]. They are relatively easy to use, allow self-calibration of the proportionality coefficient relating their electrical and mechanical properties [4], and if their resonant response is measured correctly [5], their high sensitivity enables their use as thermo-, pressure- and viscometers in all the helium fluids [4]. They have been used to study the temperature dependences of density of normal $^3$He liquid and of liquid and gaseous $^4$He [6]; cavitation in cryogenic $^4$He liquids [7, 8] or solubility of $^3$He in $^4$He at millikelvin temperature [9]. Moreover, they are also being employed (mostly in cryogenic environments) as generators and detectors of both classical [10–12] and quantum turbulence [12–18].

One of the most important characteristics of these resonators is the amount of damping they experience due to interactions with the surrounding fluid, as this can be used, e.g., to determine the transition from laminar to turbulent drag regime or to infer the fluid properties. Therefore, understanding all the damping forces is essential in order to interpret correctly the results from the numerous experiments already performed in cryogenic helium.

Dissipation due to laminar viscous drag [10, 12] or due to ballistic drag at low temperatures in $^4$He [13, 15], as well as the dissipation due to the scattering of thermal excitations in $^3$He [16, 17] are already largely understood and their dependences on most of the important physical quantities are known. In this report we try to illuminate the dissipation due to acoustic emission in $^4$He fluids, extending the works of Clubb et al. [19] and Pentti et al. [6]. In most other studies, acoustic emission by tuning forks was considered to be negligible in comparison with other losses.

We believe, however, that this assumption is valid only under certain conditions, and that acoustic emission or the interaction through sound waves might be at least partly responsible for some of the phenomena observed by us as well as by others that still remain unexplained (such as anomalously broad and time-dependent low-drive-linewidth of "standard" 32 kHz forks and their mutual interactions in pure $^4$He at very low temperature [20]). We do not intend to put forward a full comprehensive and detailed description of all the acoustics related to tuning forks. Our hope is to provide sufficiently good insight into the dissipative phenomena related to sound emission and to offer approximative estimates of the magnitude of acoustic emission in various situations. Dispersive effects of acoustic emission are beyond the scope of this paper and are not discussed here with the exception of an observed level crossing.

The paper is organized as follows—after this brief Introduction, in Sect. 2 we describe various aspects of the phenomenon of acoustic emission due to a tuning fork oscillating in a compressible fluid (mentioning special physical properties of quantum fluids) and in Sect. 3 three workable theoretical models are developed. We present our experimental data in Sect. 4 and compare them with the model predictions, while the predictions for other common oscillating structures are given in Sect. 5. Conclusions are drawn in Sect. 6.

## 2 Acoustic Emission by a Tuning Fork

Let us begin by a brief qualitative description of this rather complex phenomenon. It is known that any body oscillating in a classical viscous fluid with finite compressibility emits sound waves [21]. If we assume for simplicity that the oscillations are harmonic, then the acoustic velocity field (superimposed on the velocity field due to laminar[1] flow past the body) will depend on several factors. The most important ones are the geometry of the oscillating body, the spatial extent and properties of the surrounding fluid as well as the geometry and material properties of its boundaries. More specifically, relevant physical properties include fluid density, speed of sound and frequency of oscillations, or alternatively, wavelength of the emitted sound waves. A more detailed consideration also ought to take into account the dissipation of the emitted sound waves, affected by fluid viscosity and thermal diffusivity (responsible for damping of adiabatically propagating sound waves), and also the reflectivity and absorptivity of the boundaries, in turn depending on their acoustic impedances, heat conductivity and the Kapitza thermal resistance between the fluid and the walls.

It is readily seen that a full description of all the above mentioned processes is next to impossible, perhaps with the exception of highly advanced and sophisticated numerical simulations of special cases. For a review of computational acoustics, see Ref. [22]. Several examples of acoustic emission models can be found in Refs. [23, 24]. Therefore, we seek simplified analytically tractable working models that would give us a meaningful approximative description of the dissipation rate due to acoustic emission rather than a full account of all the relevant physical processes.

### 2.1 Acoustic Field in an Unbounded Classical Fluid

The simplest case of acoustic emission is perhaps to consider an infinitely large unbounded volume of a classical fluid with negligible damping of the propagating sound waves. In this case, all the energy content of the emitted waves is carried away from the source and it is more or less straightforward to find an analytical expression for the emission power of an oscillator, assuming certain simplifications regarding the geometry of the oscillator and neglecting the dissipation of sound waves traveling in the fluid. The general procedure is to write down the velocity potential for outward propagating spherical or cylindrical waves from a suitably chosen set of point sources representing a simplified description of such an oscillator and use it to derive the velocity and pressure fields, and from these to calculate the energy flux. As we are limited neither by geometrical considerations nor by dissipation of energy in the sound waves, we can then use approximations for the values of these fields at large distances from the oscillating body. Then, by integrating over an enclosing surface, we shall find the total emitted power.

It should be noted that, even in this textbook case, several important simplifications are already assumed. The strongest one is the representation of the oscillating body (a tuning fork) as a set of several point sources with given acoustic strengths (usually four sources [25], in a form of either lateral or longitudinal/linear quadrupole [26], see later). In reality, the oscillating prongs of the tuning fork do not act only as sources of sound waves, they also reflect and absorb them. This can be especially important if the wavelength is comparable to the dimensions of the tuning fork. Moreover, the prongs have a velocity profile along their length, which can be approximated by solving the oscillations of an ideal cantilever. Therefore, in the direction of its axis each prong

---

[1] We do not consider acoustic emission generated by turbulent flows or acoustic streaming.

should ideally be represented by an infinite number of acoustic sources with varying strengths from the base to the tip, rather than just as an acoustic dipole (thus making the entire tuning fork a longitudinal quadrupole). This simplification will become even more important if we choose to consider only the close vicinity of the tuning fork with distances from the tines comparable to the tine length, which we should keep in mind later, when describing a tuning fork placed inside its original can.

## 2.2 Effect of Solid Boundaries

If solid boundaries are present, the situation starts to look even more complicated. Strictly speaking, for calculating the acoustic fields, one should use proper solutions of the wave equation, which would be standing waves in the case of perfectly solid (and fully reflecting) walls. Note that this also means the appearance of acoustic resonances determined purely by the geometry of the container and the sound wavelength.

However, standing waves do not transport energy. A real experimental situation corresponds better to a superposition—linear combination—of propagating and standing waves, as the waves reflected off the walls will be of a lower amplitude than the incident ones, due to several factors. First, no wall is infinitely rigid and even metallic walls posses non-unity reflectivity and non-zero transmission. In other words, acoustic energy will be partly channeled into refracted waves and lost within or outside the walls. Second, additional damping of sound waves occurs at solid boundaries due to viscosity of the fluid and finite heat conductivity of the wall. The importance of these two effects depends, among other factors, on the angle of incidence of the waves. Moreover, in a real fluid, a traveling sound wave (which is adiabatic and thus includes both pressure and temperature variations) is damped due to viscous forces and thermal diffusivity and its amplitude decreases as it propagates though the fluid.

To sum up, we need to describe a situation where the velocity and pressure fields are described by a superposition of standing and outward propagating waves and depend on a number of the above mentioned parameters, but mainly on the intrinsic acoustic resonances of the closed volume under consideration, which can couple to the oscillations of the tuning fork.

## 2.3 Acoustic Emission in Superfluid $^4$He

Several potentially important differences arise when sound emission in a superfluid is considered, the main one being the existence of a new type of wave motion of the fluid—second sound—that can be thought of as waves of temperature, in which the normal and superfluid components move in anti-phase. As other nonclassical sound modes are not considered here, we therefore have mutually independent approximately *isothermal* first sound (pressure waves) and approximately *isobaric* second sound (temperature waves). The acoustic fields produced in He II by any moving body will always be a combination of these two sound modes. The emission of first sound is more or less analogical to the adiabatic sound waves in classical fluids, including similar magnitudes of sound velocity in He I and He II.

Second sound will be emitted by the tuning fork for two reasons. First, as the body moves, boundary conditions change differently for the normal (viscous liquid) and superfluid (Euler-like inviscid liquid) components, resulting in their relative motion at the frequency of oscillations, i.e., second sound. Second, if finite viscous (or ballistic at very low temperature of He II) drag forces are still present, the surface of the moving body and the surrounding layer of fluid will be heated periodically, due to these dissipative forces. Therefore, an additional second sound field will be present, due to the temperature gradient in the liquid (superimposed on a steady counterflow cooling the oscillator), but this time at double the frequency of oscillations.

It is known that an oscillating body radiates first sound much more efficiently than second sound. For a plane oscillating in a direction perpendicular to itself, the ratio of the amplitudes of the two sound waves is given by: $\beta^2 T u_2^3 / c u_1$, where $\beta$ is the heat expansion coefficient, $T$ denotes the temperature, $u_1$ and $u_2$ are the speeds of first and second sound, respectively, and $c$ is the specific heat, which is very similar for both adiabatic and isothermal processes in He II except close to the λ-point [21, 27]. As $\beta \ll 1$, $u_2 < u_1$, and in our case $T \approx 1.5$ K and $c > 500\ \mathrm{J\,kg^{-1}\,K^{-1}}$ for all temperatures above 1.3 K, we see that the ratio of amplitudes will be indeed much lower than unity. We can therefore say that the second sound emission power due to the oscillations of the tuning fork will be negligible compared to that of first sound unless enhanced by another effect, such a resonance inside the experimental cell.

Of course, both first and second sound waves travel with their own group velocities and will again have their own standing wave resonances determined by the geometry of the experimental cell. Such second sound resonances have been observed in both $^3$He–$^4$He mixtures and in pure $^4$He and are reported in Refs. [6, 9]. Based on the above considerations, we believe that unless a second sound resonance within the cell is encountered, the power lost due to emission of second sound will be much lower than the power lost because of the emission of first sound. Therefore in the following models, second sound emission is not considered quantitatively as the sharp increases in linewidth due to resonances inside the experimental cell (i.e., the only occasions at which second sound may be important) are filtered out during data processing anyway. In other words, for the purposes of calculating the emission power when away from sound resonances (and for these purposes only), we describe superfluid $^4$He as a classical compressible fluid.

## 3 Models of Acoustic Emission by Tuning Forks in a Classical Fluid

In this section, we discuss three different analytical models of acoustic emission by a tuning fork, together with their advantages and shortcomings. All these models deal with sound emission in an infinite volume of a classical fluid, but a few simple modifications will be introduced to account, at least qualitatively, for the presence of walls. The models described below are (i) 3D longitudinal quadrupole emission, (ii) emission by two infinite translationally oscillating cylinders, and (iii) 2D longitudinal quadrupole emission. The first two models are based on the works of Clubb et al. [19] and Sillitto [25], and the third one will be developed here. All these models assume potential compressible flow, so the viscous damping of sound waves is neglected. The application of these models on the quartz tuning fork is not meant to provide a rigorously accurate description of its behavior, our aim is more to illustrate

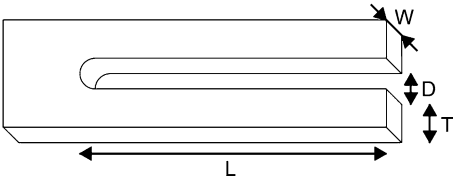

**Fig. 1** A schematic sketch of a quartz tuning fork marking its dimensions

**Table 1** Dimensions of the 38 kHz, 77 kHz and 100 kHz tuning forks used in this work (labeled F38, F77 and F100, respectively) as well as of typical 32 kHz tuning fork oscillators (F32, F38 and F100 type forks are supplied in a 3 mm diameter case 8 mm long, F32s and F77 type forks are smaller, supplied in a 2 mm diameter case 6 mm long). The dimensions have been measured using either optical (0.01 mm precision) or electron (0.001 mm precision) microscopy. For each tuning fork, the proportionality factor between the electric current and tip velocity, a, is listed, together with its quality factor, $Q_{\text{vac}}$, measured in vacuum at 4.2 K

| Fork type | $f_0$ kHz | $L$ mm | $T$ mm | $W$ mm | $D$ mm | $a$ C m$^{-1}$ | $Q_{\text{vac}}$ |
|---|---|---|---|---|---|---|---|
| F32 | 32 | 3.79 | 0.589 | 0.300 | 0.308 | $2.3 \times 10^{-5}$ | $6.3 \times 10^{5}$ |
| F32s | 32 | 2.53 | 0.249 | 0.100 | 0.127 | $3.4 \times 10^{-6}$ | $1.0 \times 10^{6}$ |
| F38 | 38 | 3.41 | 0.599 | 0.330 | 0.306 | $1.6 \times 10^{-5}$ | $6.5 \times 10^{5}$ |
| F77 | 77.5 | 1.93 | 0.402 | 0.340 | 0.206 | $1.3 \times 10^{-5}$ | $7.0 \times 10^{5}$ |
| F100 | 100 | 1.98 | 0.585 | 0.335 | 0.302 | $2.1 \times 10^{-5}$ | $6.2 \times 10^{5}$ |

the basic features of acoustic emission by tuning forks, providing estimates of the emitted acoustic power that are correct at least in their orders of magnitude. In due course we shall also test these models against our experimental data.

Throughout the rest of this paper, the fork dimensions $T$, $L$, $W$, $D$ will be used as introduced in Fig. 1; see Table 1 for their numerical values. Also the following set of symbols will be used: $i$ as the imaginary unit, $\rho$ as the fluid density, $c$ as the sound velocity, $\omega$ as the angular frequency of oscillation, $k$ as the wavenumber related to the sound waves, $U$ as the velocity amplitude of the tip of the prongs and $L_{\text{e}} = 0.3915L$ as an *effective emitting length* of a prong, taking into account at least roughly the varying velocity profile along the length of the prong. The numerical coefficient corresponds to the ratio of the average velocity along the prong to the tip velocity, as follows from the Euler beam equation [28]. This value remains the same for all dimensions of the tuning forks if the fundamental bending mode is considered and as long as the assumptions of Euler beam theory for a thin dissipationless cantilever remain at least approximately valid.[2]

## 3.1 Description of Acoustic Emission Within Existing Models and Their Extension

A brief description of the two known models is presented below and we restate the resulting acoustic emission powers in two forms—first, using a more general expression (in practice an infinite sum of Bessel functions) and second, after taking the long

---

[2] The effective emitting length approximation can also be justified only if the entire problem of acoustic emission is understood as linear.

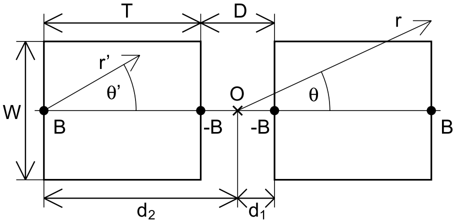

**Fig. 2** The tuning fork (view of the tips of the prongs) represented as a longitudinal quadrupole. The variables $r$, $\theta$ belong to the universal coordinate system of the entire quadrupole with origin at O, while the primed variables belong to individual acoustic monopoles

wavelength limit, i.e., "wavelength ≫ relevant oscillator dimensions", which means mathematically that the arguments of all relevant Bessel functions must be much smaller than unity.

We begin with looking at the most commonly used model of acoustic emission by tuning forks , which describes the tuning fork as a longitudinal quadrupole oscillating in a 3D fluid. A full and detailed derivation of the pressure and velocity fields as well as the predicted emission power can be found in Ref. [25], here we only outline its main ideas. We begin by writing the velocity potential for an outward propagating wave due to an acoustic monopole in 3D (a pulsating sphere reduced to a point source):

$$\Phi_{3\mathrm{D},1}(r',t)=\frac{Be^{i(kr'-\omega t)}}{4\pi r'}, \tag{1}$$

where $r'$ is the distance from the monopole and $B$ is the acoustic source strength, defined as the product of emitting area times the (normal) velocity amplitude, in our case $B=WL_\mathrm{e}U$. The longitudinal quadrupole used to model the tuning fork then consists of two point sources with strength $B$ and two with strength $-B$ arranged according to Fig. 2. Using identities for displaced spherical harmonics [29], we arrive at the velocity potential of the entire quadrupole in the coordinate system with its origin in the center of mass of the quadrupole $(r,\theta)$:

$$\Phi_{3\mathrm{D}}(r,\theta,t)=\frac{iBke^{-i\omega t}}{2\pi}\sum_{\substack{m=0\\ even}}^{\infty}(2m+1)P_m(\cos\theta)h_m(kr)[j_m(kd_2)-j_m(kd_1)], \tag{2}$$

where $P_m(\cos\theta)$ are Legendre polynomials, $h_m(kr)$ are spherical Hankel functions, $j_m(kd_i)$ are spherical Bessel functions, and $d_1=D/2$, $d_2=D/2+T$. The potential is independent of the azimuthal angle, $\varphi$, due to axial symmetry around the quadrupole axis (which is, of course, not valid for the actual tuning fork). The emission power using the notation of tuning fork dimensions results as follows:

$$P_{3\mathrm{D}}=\frac{\rho\omega W^2L_\mathrm{e}^2U^2}{2\sqrt{2\pi d_1d_2}}\sum_{\substack{m=0\\ even}}^{\infty}(2m+1)\left[j_m(kd_2)-j_m(kd_1)\right]^2; \tag{3a}$$

$$P'_{3\mathrm{D}} = \frac{\rho\omega k^5 W^2 T^2 (T+D)^2 L_\mathrm{e}^2}{40\pi} U^2 = \frac{\rho\omega^6 W^2 T^2 (T+D)^2 L_\mathrm{e}^2}{40\pi c^5} U^2, \tag{3b}$$

where (3b) is the simplification of (3a) in the long wavelength limit.

The main advantage of this model, i.e., the fact that it gives a full 3D description of the acoustic field, is unfortunately also related to its most severe drawback. By considering the tuning fork as a set of collinear point sources in 3D space, an assumption is already implied that its length and width are much shorter than the wavelength, $L, W \ll \lambda$. Note that this is true even before taking the "long wavelength" limit, which applies to other dimensions, namely $T$ and $D$. By estimating the wavelength for a typical 32 kHz tuning fork at 4.2 K we get $\lambda \approx 5.6$ mm, which increases to about 7.5 mm at lower temperatures. This is still larger than the length of a prong of a typical 32 kHz tuning fork, but of the same order of magnitude and definitely comparable. The ratio of the wavelength to prong length is even worse for the 77 kHz and 100 kHz tuning forks discussed in Sect. 4, the consequence being that this model tends to underpredict the emission power.

This was pointed out already by Clubb et al. [19] for a simplified version of the same model, with the dependence on tuning fork geometry limited only to considering $W$ and using slightly different approximations than Ref. [25]. Clubb et al. suggested to use a different model instead—two infinite cylinders performing transverse translational oscillations in antiphase.

Again, we begin by the velocity potential around a single infinite transversely oscillating cylinder, which can be derived based on the calculations in Ref. [21]:

$$\Phi_{\mathrm{C},1}(r', \varphi, t) = \frac{\pi R^2}{2i} kUH_1(kr') \cos\varphi\, e^{-i\omega t}, \tag{4}$$

where $R$ is the radius of the cylinder and $H_1(kr)$ is the first order cylindrical Hankel function. The potential around the second cylinder has to be taken with a minus sign, as they oscillate in antiphase. This time we express $\cos\varphi$ as a sum of complex exponentials and use the identities for displaced cylindrical harmonics, arriving at:

$$\Phi_\mathrm{C}(r, \varphi, t) = \frac{\pi R^2 kUe^{-i\omega t}}{2i} \sum_{\substack{m=-\infty \\ odd}}^{\infty} J_m(kF)\left[H_{m+1}(kr)e^{i(m+1)\varphi} - H_{m-1}(kr)e^{i(m-1)\varphi}\right] \tag{5}$$

for both cylinders, where $J_m(kF)$, $H_m(kr)$ are cylindrical Bessel and Hankel functions, respectively, and $F = (T+D)/2$ is the distance of the center of mass of one cylinder from the origin placed exactly between the cylinders. This potential yields the following emission power:

$$P_\mathrm{C} = \rho\omega\pi^2 R^4 k^2 L_\mathrm{e} U^2 \sum_{\substack{m=-\infty \\ odd}}^{\infty} J_m(kF)\left[J_m(kF) - J_{m-2}(kF)\right]; \tag{6a}$$

$$P'_\mathrm{C} = \frac{3}{16}\rho\omega k^4 W^2 T^2 (T+D)^2 L_\mathrm{e} U^2 = \frac{3}{16}\frac{\rho\omega^5 W^2 T^2 (T+D)^2 L_\mathrm{e}}{c^4} U^2, \tag{6b}$$

where in (6b) we took the long wavelength limit and replaced the cross-section of the cylinder, $\pi R^2$, by the cross-section of a prong, $WT$. Dimensionally, this result is in agreement with Ref. [19], however, different prefactors were obtained. The difference in the prefactors arises from our usage of velocity amplitude, $U$, instead of mean square velocity, $\langle u^2 \rangle$, used in Ref. [19] and from a different method of replacing the cylinder diameter with tuning fork dimensions.[3]

This 2D model in its full form (6a) takes the relationship between the tuning fork dimensions and the wavelength to the opposite extreme—the length of the cylinders is assumed to be infinite, while other dimensions are represented more or less correctly, although cylindrical symmetry of each prong is forced artificially. This means that we are now operating in the $L \gg \lambda$ limit and the emission power might be overpredicted, although this effect would probably be smaller than the underprediction of the first model, especially for our 77 kHz and 100 kHz tuning forks.

Comparing these two models, we might say that they can be treated as opposing limiting cases and that the actual emission power of the tuning fork should lie somewhere between the respective predicted values. Please note that in the experimental part of this paper, all the emission powers are scaled by fitting parameters and therefore appear comparable in the presented figures. See Sect. 4 for the values of these parameters and comparison of the individual predicted emission powers.

### 3.2 2D Longitudinal Quadrupole Emission

In this section, we present the derivation of the last model of acoustic emission by tuning forks—2D longitudinal quadrupole emission. The aim in developing this model is to overcome the difficulties with the previous models, that is, to avoid the wavelength vs. prong length issue of the 3D quadrupole model, but at the same time to avoid introducing cylindrical symmetry of both prongs artificially, and also to provide a reasonable basis for comparison, lying between the "extreme" cases represented by the two above mentioned models.

Although we do not expect the result of this new 2D model to be largely different from the infinite cylinders model (also 2D), we hope that it might provide a more accurate description of acoustic emission, especially for the 77 kHz and 100 kHz tuning forks used in our experiment. The derivation of this model is given in greater detail, since we are not aware of any literature that contains the same in its entirety and also to illustrate the methodology, which was also used in a very similar manner to derive the emission powers from the first two models.

Again, we begin by considering the velocity potential of an outward propagating wave due to a 2D acoustic monopole (a pulsating cylinder reduced to a point source), which can be derived based on the textbook examples in Ref. [21]:

$$\Phi_{2D,1}(r', t) = \frac{B}{4i} H_0(kr') e^{-i\omega t}, \tag{7}$$

where B is again the acoustic source strength, equal to the (normal) velocity amplitude multiplied by the emitting line length, which is the 2D equivalent of the emitting

---

[3] We also believe there was an accidental misprint in the denominator of (5) in Ref. [19].

area in 3D; in this case $B = WU$. Similarly to the 3D quadrupole model, we now assume four acoustic sources arranged as in Fig. 2, two with strength $B$ and two with $-B$. Combining their potentials using identities for displaced cylindrical harmonics [29], we arrive at:

$$\Phi_{2\mathrm{D}}(r,\varphi,t) = \frac{B}{2i} e^{-i\omega t} \sum_{\substack{m=-\infty \\ even}}^{\infty} H_m(kr) e^{im\varphi} \left[ J_m(kd_1) - J_m(kd_2) \right]. \tag{8}$$

The next step is to calculate the velocity and pressure fields according to:

$$\mathbf{v}(r,\varphi,t) = \nabla\Phi(r,\varphi,t); \qquad p(r,\varphi,t) = -\rho \frac{\partial\Phi(r,\varphi,t)}{\partial t}. \tag{9}$$

Eventually, we will also need to calculate the mean sound intensity, **I**, and the emission power, $P$, according to:

$$\mathbf{I}(r,\varphi) = \frac{1}{2} \mathrm{Re}\{p(r,\varphi,t)\ \mathbf{v}^*(r,\varphi,t)\}; \tag{10}$$

$$P = L_\mathrm{e} \oint \mathbf{I}(r,\varphi) \cdot \mathbf{dl} = r\, L_\mathrm{e} \int_0^{2\pi} I_r(r,\varphi)\, \mathrm{d}\varphi, \tag{11}$$

where the path integral is taken over a closed circular loop and **dl** is an outward pointing vector normal to the path segment and its magnitude is equal to the length of the same segment. It follows that we will only be interested in the radial component of the mean sound intensity (and of the velocity field) and, more specifically, only in those terms that do not vanish upon integration over the full range of the polar angle.

The potential in (8) yields the following radial velocity and pressure fields:

$$v_\mathrm{r}(r,\varphi,t) = \frac{Be^{-i\omega t}}{2ir} \sum_{\substack{m=-\infty \\ even}}^{\infty} [mH_m(kr) - kr\, H_{m+1}(kr)][J_m(kd_1) - J_m(kd_2)] e^{im\varphi}; \tag{12}$$

$$p(r,\varphi,t) = -\frac{1}{2} \rho\omega B e^{-i\omega t} \sum_{\substack{m=-\infty \\ even}}^{\infty} H_m(kr) e^{im\varphi} [J_m(kd_1) - J_m(kd_2)]. \tag{13}$$

The radial component of the mean sound intensity is then:

$$\begin{aligned} I_\mathrm{r}(r,\varphi) = -\frac{\rho\omega B^2}{8r} \mathrm{Im}\Bigg\{ &\sum_{\substack{m=-\infty \\ even}}^{\infty} \sum_{\substack{n=-\infty \\ even}}^{\infty} H_n(kr)[mH_m^*(kr) - kr\, H_{m+1}^*(kr)] \\ &\times [J_n(kd_1) - J_n(kd_2)][J_m(kd_1) - J_m(kd_2)] e^{i(n-m)\varphi} \Bigg\}. \end{aligned} \tag{14}$$

To eliminate the double sum, we remember that the angular parts of cylindrical harmonics, which is the only $\varphi$-dependent term in (14), are orthogonal on the interval $[0, 2\pi]$:

$$\int_0^{2\pi} e^{in\varphi} e^{-im\varphi}\,\mathrm{d}\varphi = 2\pi\delta_{m,n}. \tag{15}$$

It therefore follows (as the Bessel functions have real values here, and the product of $H_m$ and $H_m^*$ is also real) that the emission power can be expressed from (11) as:

$$P = \frac{\pi\rho\omega kr B^2 L_\mathrm{e}}{4} \sum_{\substack{m=-\infty \\ even}}^{\infty} [J_m(kd_1) - J_m(kd_2)]^2 \mathrm{Im}\{H_m(kr)H_{m+1}^*(kr)\}. \tag{16}$$

From the law of conservation of energy it follows that the radiation power (if dissipation is neglected) cannot depend on $r$. For the purposes of this calculation, we can therefore replace the Hankel functions by their asymptotics for $r \to \infty$:

$$H_m(kr)\,H_{m+1}^*(kr) \approx \sqrt{\frac{2}{\pi kr}}\; e^{i(kr-\frac{m\pi}{2}-\frac{\pi}{4})}\sqrt{\frac{2}{\pi kr}}\; e^{-i(kr-\frac{(m+1)\pi}{2}-\frac{\pi}{4})} = i\frac{2}{\pi kr}. \tag{17}$$

Using (17) and substituting $B = WU$, we finally arrive at the emission power:

$$P_{2\mathrm{D}} = \frac{\rho\omega W^2 L_\mathrm{e} U^2}{2} \sum_{\substack{m=-\infty \\ even}}^{\infty} [J_m(kd_1) - J_m(kd_2)]^2. \tag{18a}$$

In the long wavelength limit (we take the lowest order term of the Taylor expansion of the Bessel functions), and substituting $d_1 = D/2$ and $d_2 = D/2 + T$, this reduces to:

$$P'_{2\mathrm{D}} = \frac{3}{64}\rho\omega k^4 W^2 T^2 (T+D)^2 L_\mathrm{e} U^2 = \frac{3\,\rho\omega^5 W^2 T^2 (T+D)^2 L_\mathrm{e}}{64 c^4} U^2. \tag{18b}$$

It is apparent that in the long wavelength limit, the emission power given by the 2D quadrupole model is always exactly four times smaller than the one predicted by the cylinders model. However, without taking this limit, the relation between these two models is not so straightforward as they scale slightly differently with the wave vector, and therefore also with the sound velocity and frequency of oscillations.

### 3.3 Application of Acoustic Emission Models

There are several important issues that should be kept in mind when applying the above mentioned models to interpret various cryogenic experiments with quartz tuning forks. First of all, the models are derived for an infinite volume of dissipationless fluid, and we have to modify them to take into account the fact that tuning forks vibrate in a closed volume of helium.

When the resonant frequency of the tuning fork matches some acoustic resonance of the cell (acting as a 3D sound resonator), the signal is suppressed, as the same amount of supplied power is now divided among several damped modes of coupled oscillatory motion, which can be seen in the tuning fork's spectra as multiple resonance peaks, provided they are strong enough, see Figs. 3 and 4 in Sect. 4 for a practical example. Such data would generally show "increased linewidths" (also Figs. 7, 8, 9 in Sect. 4), especially due to the fact that commonly used processing software usually attempts to fit these complicated spectra with a single Lorentzian function. As the best Lorentzian fit does not have any physical meaning in these situations, we merely use this kind of data as an indication of an acoustic resonance present inside the cell (be it first or second sound resonance), but we do not take the numerical values of the linewidth into account in any quantitative way.

Having thus identified and separated the acoustic resonances of the cell, we focus only on the rest of the data (the "floor" in Figs. 7, 8, 9 in Sect. 4). Then we find that we also need to introduce a parameter that describes the energy balance at the boundaries. We have therefore considered the power transmission coefficient, $T(\theta)$, for plane waves propagating in liquid helium incident on a planar surface of a wall (the tuning fork capsule used is made of aluminium) at an angle $\theta$. The power transmission coefficient is determined [30] as:

$$T(\theta) = \frac{4\rho_{\mathrm{He}}\rho_{\mathrm{Al}}c_{\mathrm{Al}}\cos\theta\sqrt{c_{\mathrm{He}}^2 - c_{\mathrm{Al}}^2\sin^2\theta}}{\left(\rho_{\mathrm{Al}}c_{\mathrm{Al}}\cos\theta + \rho_{\mathrm{He}}\sqrt{c_{\mathrm{He}}^2 - c_{\mathrm{Al}}^2\sin^2\theta}\right)^2}. \tag{19}$$

In the simplest case of normal incidence, it can be expressed in terms of the specific acoustic impedances of helium and the wall material (aluminium), $Z_{\mathrm{He}}$ and $Z_{\mathrm{Al}}$, respectively:

$$T(0) = \frac{4Z_{\mathrm{Al}}Z_{\mathrm{He}}}{(Z_{\mathrm{Al}} + Z_{\mathrm{He}})^2}, \tag{20}$$

where the individual specific acoustic impedances are defined as the products of the speed of sound and the density of the given media. The values we use for aluminium are $\rho_{\mathrm{Al}} = 2700\ \mathrm{kg\,m^{-3}}$, $c_{\mathrm{Al}} = 6420\ \mathrm{m\,s^{-1}}$.[4] These depend mainly on the exact composition of the aluminium alloy used and on the method of preparation of the material, and can be considered pressure and temperature independent in our experimental range between 0 and 25 bar, and 1.3 and 4.2 K, respectively. On the other hand, the relevant helium properties vary considerably with temperature and pressure and are therefore calculated accurately for each individual data point using the HEPAK software package [31, 32].

Even though the exact geometry of the experiment is rather complicated, we still believe that the actual ratio of the transmitted energy will be roughly proportional to the integral of the power transmission coefficient from zero angle of incidence to the

---

[4] The exact values of aluminium density and speed of sound depend significantly on the method of preparation. We use the values provided at www.signal-processing.com for rolled aluminium.

rather small (≈3 degrees) critical angle for total internal reflection, $\theta_{\mathrm{C}}$, which is given by:

$$\theta_{\mathrm{C}} = \arcsin\left(\frac{c_{\mathrm{He}}}{c_{\mathrm{Al}}}\right), \tag{21}$$

as it is easy to imagine that acoustic waves will arrive at the walls at angles differing by much more than just $\theta_{\mathrm{C}} \approx 3$ degrees. The mentioned integral is found to depend on temperature and pressure in a nontrivial manner due to the changing acoustic properties of liquid helium. In this approach, we have to assume that the angular distribution of the incident waves (when decomposed to plane wave components) is roughly constant between 0 and $\theta_{\mathrm{C}}$, or at least, even if it does exhibit some angular dependence in this small range of available angles, that the character of the dependence does not change dramatically with temperature or pressure in the explored experimental range.

Due to the enormous acoustic impedance mismatch between liquid helium and aluminium, $Z_{\mathrm{Al}} \gg Z_{\mathrm{He}}$, and the small value of the critical angle ($\sin\theta \approx \theta$, $\cos\theta \approx 1$ for $\theta < \theta_{\mathrm{C}}$) or, in other words, due to the large Kapitza resistance [33] of the boundary, $T(\theta)$ can be approximated by an elliptical function:

$$T(\theta) = 4\frac{\rho_{\mathrm{He}}}{\rho_{\mathrm{Al}}}\sqrt{\left(\frac{c_{\mathrm{He}}}{c_{\mathrm{Al}}}\right)^2 - \theta^2}. \tag{22}$$

The above mentioned integral can then be expressed as the area under the quarter-ellipse, $(\pi/4)\,T(0)\theta_{\mathrm{C}}$. The emission power given by the respective models is then multiplied by this value, taking into account at least approximately the effects of the boundaries. Note that the obtained emission power is still fully determined only by the experimental conditions.

When this approach is subjected to a careful analysis, one would find that it only considers a singular transmission/reflection on the solid boundary and therefore neglects the influence of multiple reflections. In reality, what happens will be similar to the following scenario. First, a wave of some undetermined 3D profile is emitted by the tuning fork. It propagates toward the solid boundary (experiencing low damping in He), where it is partly transmitted, partly reflected, and partly dissipated. The reflected wave then returns to the tuning fork, where it is partly absorbed, partly scattered, and partly dissipated again. The scattered wave will eventually reach the outer boundary again and the whole process will be repeated until all the energy in the wave is re-absorbed by the tuning fork, transmitted through the solid boundary or dissipated into heat. A full treatment of these phenomena (even neglecting dissipation) seems unfeasible to us at the moment even in terms of a cylindrically symmetrical 2D model, because of the complicated geometry of the actual experiment as the dimensions of the tuning fork are comparable both with the diameter of its capsule and with the wavelength of the acoustic radiation.

It is, however, instructive to estimate the importance of multiple reflections by considering a simplified 1D model with an acoustic source located at one end of a resonator and a partly transmitting boundary at the other. Complementing it with the proper boundary conditions (velocity matches that of the source at its surface, and the ratio of the amplitudes of the incident and reflected waves on the boundary is given by the finite amplitude reflectivity coefficient) one can arrive (i) at the actual resonance frequencies of such a system, and (ii) at the energy flow through the solid boundary. It follows that the transmitted energy depends on tuning/detuning of the source to/from the resonance of the system, as can be expected. For example, one finds that in resonance, the transmitted energy is enhanced by a large factor inversely proportional to the (rather small) power transmission coefficient of the boundary, compared to the case exactly between resonances. This is qualitatively in agreement with the experiment—the dissipation was observed to increase significantly when a resonance of the experimental volume was encountered. Another important result follows from this simplified 1D model—by considering the case exactly between resonances, one may find that the transmitted power differs from the one determined by the above mentioned single-reflection approach only by a constant factor of two. While the magnitude of this constant factor may generally change with the dimensionality of the model problem, it will still remain a constant value for any selected number of dimensions in which the model is formulated, independent of any experimental conditions, such as the speed of sound (and by extension temperature and pressure), as long as we stay far away from all resonances (analogically to being exactly between them in the simplified 1D case).

Therefore, as the complex geometry of the experiment complicates its exact description, we take the resulting emission power according to the suggested single-reflection approach for each of the three models and multiply it by an arbitrary constant, which we consider as the only fitting parameter for each model. The values of this multiplicative constant then differ among the three models, but are not changed for different experiments interpreted using the same model. The final value of the emission power is then used to calculate the corresponding drag force and using the effective mass of the tuning fork prong as defined in [4] also to arrive at the corresponding increase in linewidth of the tuning fork due to acoustic emission, which is then added to the linewidth due to viscous drag (also containing a multiplicative constant as a fitting parameter) and compared to the experimental data.

Another issue relates to the ratio of tuning fork dimensions and the wavelength, especially to the choice of the final formula used to calculate the emission power within each model. While for the common 32 kHz forks, the simplified (long wavelength limit) version is quite sufficient, giving roughly 5% relative errors when compared to the full formula, it fails badly for our higher frequency (77 kHz and especially 100 kHz) forks, where it may result in errors as large as 50%. In this work, we therefore use the full form of all the models for calculating the emission powers. A numerical calculation shows that it is usually sufficient to take into account only a few terms around $m = 0$ in the infinite series to reduce the error below 1% (two or three terms in both directions of $m = 0$ are usually sufficient).

## 4 Experimental Results and Discussion

All the results presented here were obtained using tuning forks placed inside a pressure cell of 20 mm diameter located inside a glass cryostat. The cell was connected via a capillary to a pressurizing system utilizing a carbon cold trap. Both the cell

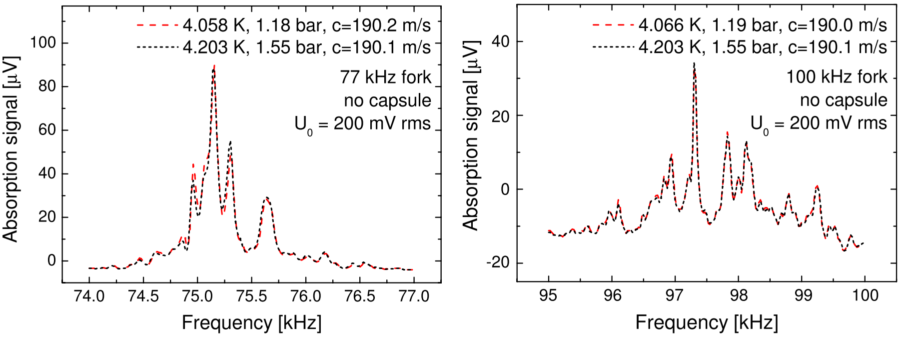

**Fig. 3** (Color online) Sample spectra obtained with open tuning forks in our cylindrical pressure cell of 20 mm diameter. Under stable temperature and pressure, the spectra were also stable and very reproducible; within the resolution of this figure they appear identical. Here, they reproduce very closely even though the two temperatures listed in the graphs differ, as the speed of sound and therefore wavelength does not change much between them, due to an according change in pressure, which was achieved simply by keeping the pressure cell volume closed during cooldown. The fact that the spectra seem to reproduce under different experimental conditions linked only by very close sound velocities serves as evidence that the extra peaks indeed result from acoustic phenomena. In contrast, resonances measured in vacuum at 4.2 K (not shown here) display only a single peak that can be fitted by a Lorentzian function with very good accuracy. For comparison, at 4.2 K, the 77 kHz tuning fork used here has a vacuum linewidth as low as 58 mHz ($Q > 10^6$; measured using an excitation voltage of 20 mV rms attenuated by 40 dB)

and the cold trap could be shut off using manually operated high pressure valves. The pressure inside the cell was measured using an MKS Baratron with a 5000 Torr range, while bath temperature was calculated based on saturated vapor pressure which was measured by a more sensitive Baratron model with a range of 1000 Torr. The electrical part of the setup consisted of an Agilent waveform generator that provided the driving voltage, a SR-830 lock-in amplifier operated in voltage mode that was used to detect the electrical signal, and an I/V converter made in Lancaster and described in Ref. [5] with a gain setting of 1000 V/A. The exact magnitude of the driving voltage was also monitored using a Keithley digital multimeter.

The first hint of acoustic emission and coupling to resonant sound modes can already be seen when recording a single spectrum of a high frequency tuning fork oscillating in liquid helium, such as the illustrative examples in Fig. 3, which were obtained with "open" tuning forks, i.e., with their original capsules removed, or in Fig. 4, with the forks inside their capsules. We stress that if the experimental conditions, i.e., temperature and pressure in the cell, are controlled and kept constant, the spectra are perfectly reproducible within experimental accuracy when the frequency of the drive is swept many times in either direction. Also, the complicated pattern in these spectra seems to depend only on the sound velocity that can be calculated for the relevant experimental conditions (temperature and pressure).

Although it is hard to make practical use of the shape of such a complicated spectrum, it can provide us with general information on the qualitative level, in that sound waves within the surrounding medium indeed do affect the behavior of the tuning forks. The number of the peaks observed can also be used as an estimate of the number of resonant sound modes coupling to the resonance of the tuning fork, although it should be kept in mind that even in spectra showing only a single Lorentzian peak

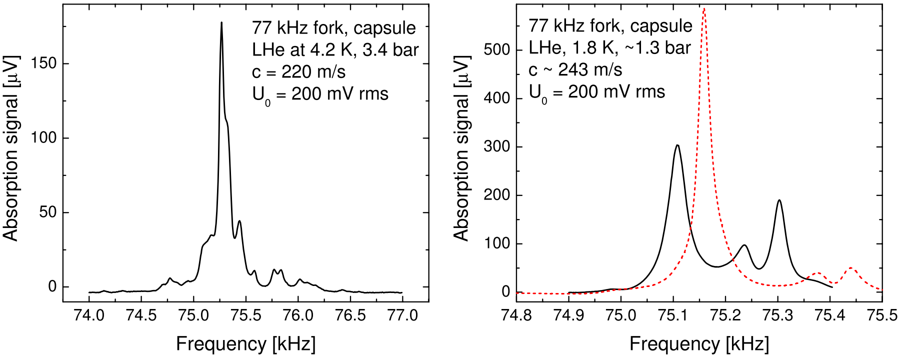

**Fig. 4** (Color online) Spectra obtained with tuning forks inside their original capsules. These already exhibit a much simpler structure, as less acoustic modes fit inside the small 2 mm capsule than into the 20 mm pressure cell. The *right panel* shows two spectra obtained under similar conditions differing only by a small change in pressure (21 mbar). However, this small difference is sufficient to shift the frequencies of acoustic resonances as is shown in the graph. The (*red*) *dashed line* represents the situation where the acoustic resonances are still far from the tuning fork resonance, while the (*black*) *solid line* shows the acoustic modes already very close to the resonance of the tuning fork itself (refer to Fig. 6 for more details on interaction of the tuning fork resonance with acoustic ones). In the latter case, the response of the tuning fork itself appears suppressed compared to the previous case, as the supplied power is now distributed more evenly among the different types of damped motion. It is also worthwhile to notice that an attempt to fit the latter spectrum with a single Lorentzian function would also result in a higher fitted value of linewidth, which would, however, under the given circumstances, have no direct physical meaning

at the first sight, small hidden features due to acoustic resonances may be present as well. We believe that the complicated form of these spectra relates to the complicated geometry of the tuning forks and their surroundings. For example, in the case of Fig. 3, the tuning forks were placed inside a cylindrical pressure cell with a diameter of 20 mm, and the sound wavelengths were about 3.5 mm and 2.5 mm for the 77 kHz and 100 kHz tuning forks, respectively, while in Fig. 4, the 77 kHz tuning fork inside its original capsule of about 2 mm diameter exhibits much simpler spectra. The figures also suggest that the acoustic fields inside the cell form a complicated pattern due to the nonsymmetric positions of the tuning forks and multiple reflections of the emitted sound waves. Let us add for completeness that these forks driven at room (RT) or low temperature in vacuum display the usual narrow (linewidth of order 1 Hz at RT, and about 100 mHz at 4.2 K, typical for most of commercially produced forks) Lorentzian response, so the complicated spectra obtained in cryogenic helium indeed seem to be a consequence of the interaction with the surrounding media by the emission of sound.

It should be stressed that the spectra become simpler if the tuning forks are kept inside their much smaller original cans (diameter of about 3 mm or smaller), or if the speed of sound (and therefore the sound wavelength) is increased, by changing the temperature and/or pressure. This was the case of the spectra measured in a cell attached to the mixing chamber of a dilution refrigerator in Kharkov, Ukraine [13], which already had the form of single peaks only (or at least approached it with reasonable accuracy) and therefore could be fitted by a single Lorentzian function. The resulting damping (expressed in terms of the resonant linewidth) is plotted in Fig. 5

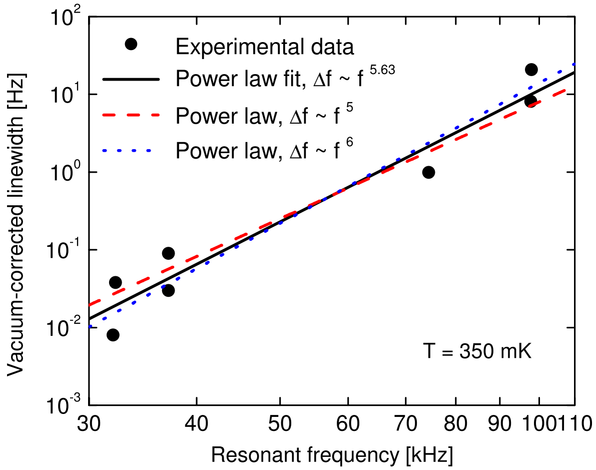

**Fig. 5** (Color online) Linewidth (with its low temperature vacuum value subtracted) plotted versus the resonant frequency of different tuning fork oscillators at very low temperature. The high exponent in the power law fit is a clear indication of acoustic emission. The (*black*) *solid line* is a full power law fit, the (*red*) *dashed line* is a fit with the exponent fixed at 5 and the (*blue*) *dotted line* is the same with the exponent fixed at 6. Note that at 350 mK, ballistic drag due to phonon scattering is negligible with respect to the acoustic drag force for the high frequency forks. For the 32 kHz and 38 kHz forks, we estimate these to be comparable in orders of magnitude, see Sect. 6

for tuning forks oscillating at their respective resonant frequencies of 32, 38, 77 and 100 kHz. This very steep frequency dependence serves as direct proof of acoustic emission playing an important part at low temperatures in $^4$He. The power law fit yields an exponent of about 5.6, which is between 5 and 6 as predicted from the above discussed 2D and 3D models, respectively, and largely differs from the value of 1/2 expected due to the viscous drag force [12]. As the ordinate variable in Fig. 5 is the vacuum-corrected linewidth, it follows that the frequency dependence of the amount of damping is not normalized for the slightly different geometries and the exact sizes of the individual tuning forks, although generally, dependences on tuning fork dimensions are to be expected from the models described in Sect. 3. This is because it would be very difficult to take into account at the same time also the differing geometry of the surroundings of the tuning forks in two successive experiments, which comprise the data shown in Fig. 5. We therefore use the data corrected only for the vacuum linewidth as presented in Fig. 5 as they are perhaps more reliable than the data normalized for tuning fork geometries would be.[5]

Next, we examine in greater detail what happens when the resonance of the tuning fork is crossed by an acoustic resonance determined by its surroundings (primarily by the geometry of the experimental cell). Both these resonances move in the frequency domain due to changing experimental conditions. For this purpose, a measurement taken in cryogenic He gas at 4.2 K (enabling an easy control of pressure) serves very

---

[5] An attempt to take into account the slightly differing dimensions of the tuning forks as per the models actually resulted in an exponent even higher than 6, allowing us to conclude once again that the importance of acoustic emission is indeed firmly established.

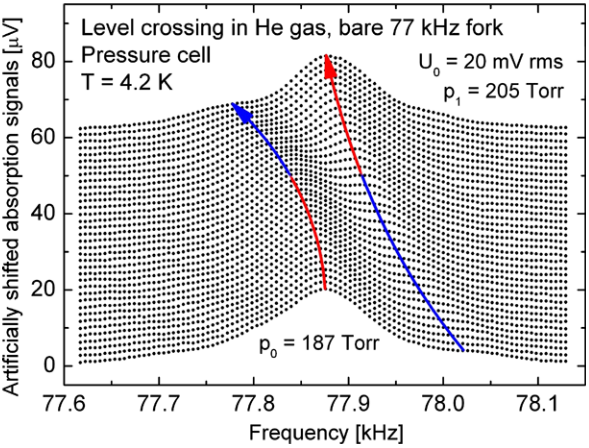

**Fig. 6** (Color online) The gradual appearance and disappearance of a level crossing event is shown for an experiment in He gas at 4.2 K. Similar events were observed in both normal liquid and superfluid helium, but in He gas it is much easier to control the experimental conditions, and therefore the studied level crossing is seen more clearly. During this event, the resonance of the tuning fork becomes gradually coupled to and decoupled from an acoustic resonance of the pressure cell. Strictly speaking, one cannot say which peak belongs to the resonance of the tuning fork and which to the acoustic mode during this process, as both resonances are the result of coupling between these two types of oscillatory motion. However, for the sake of clarity, we can tentatively describe the scenario as follows. At the beginning, while the acoustic peak (*blue arrow*) moves in from the right, the resonance of the tuning fork (*red arrow*) stays almost constant. As they approach each other, the level splitting due to coupling will become more apparent, manifesting as a "repulsion" between the peaks. Eventually, the peaks will become equal in amplitude, at which point, each peak represents both types of motion (tuning fork oscillation and acoustic waves) equally. A literal crossing is avoided, as at this point the peaks exchange their roles. Afterwards, the left one belongs predominantly to the acoustic mode and continues to drift to the left, while the right one can be associated more readily with the resonance of the tuning fork and stays more or less at a constant frequency, only slowly returning to its original position

well, although a similar effect was also observed in He liquids while slowly varying pressure and/or temperature. However, since the spectrum of the high frequency tuning forks is usually much more complicated in He liquids unless special care is taken, such data are less illustrative. The results from He gas at 4.2 K are plotted in Fig. 6, showing an acoustic peak moving past the tuning fork resonance, as the pressure is increased from 187 to 205 Torr. The amplitude of such peaks at each instant is affected by the resonance of the tuning fork itself—when they are far away from the resonance they are small, as they approach the tuning fork's maximum amplitude, they grow significantly and again gradually disappear as they move away.

During these measurements, the relative change of the resonant frequency of the tuning fork can be expected to be about $6 \times 10^{-5}$ (about 4.7 Hz), see Ref. [4] for its dependence on the fluid density, while the relative change in the frequency of the acoustic resonances should be $3.4 \times 10^{-3}$ (about 260 Hz), as this corresponds to the relative change of the speed of sound between the initial and final pressures. This fact supports the interpretation that a coupled acoustic resonance peak is indeed observed passing by the (suppressed) tuning fork resonance. Therefore, during experiments with imperfect thermodynamical stability (variations of temperature, pressure, or any other quantity affecting the sound wavelength or the acoustic boundary conditions), similar level crossings may be observed. Their occurrence will depend on the total magnitude of the change of the acoustic fields inside the experimental volume regardless of the rate of these variations, even if all the properties of the tuning fork itself are assumed perfectly constant.

For example, if small hidden peaks present in the signal are moving across the resonance of the tuning fork, the linewidth as obtained from a Lorentzian fit would be seen to increase when the two resonances start to overlap and decrease again when they move apart. At the same time the fitted resonant frequency would first move in one direction from its real value, then cross this value again, moving to its other side (as the extra acoustic peak moves across the resonance of the tuning fork), before relaxing again to its original value as the acoustic peak moves further away and decouples gradually. It is an open question if temporal changes in observed low-drive-linewidth of the tuning fork at very low temperature under apparently very stable experimental conditions such as observed by the Lancaster group [20] could be explained due to the slow drift of remnant quantized vortices in the cell, as the associated superflow may slightly alter the acoustic resonant conditions, leading in turn to time-dependent losses due to acoustic emission.

It should be noted though that reproducibility of level crossings was not ascertained in this particular experiment as even very small changes in the bath temperature may lead to significant drifting of acoustic resonance peaks. The drifting would be observable very clearly on the scale of Fig. 6, unless compensated by proper adjustments of pressure to achieve the same sound velocity. We hope the reader understands that, in this case, achieving a level of reproducibility of the frequency spectra as presented above in Fig. 3, would be a highly nontrivial task requiring a series of delicate adjustments of both temperature and gas pressure inside the cell. Attempting this in a glass cryostat with a rather simple manually controlled pressurizing system could prove quite unpractical, as any sudden pressure change inside the cell also upsets the temperature therein and thermal relaxation usually takes about 10–20 minutes. Nevertheless, a hint on reproducibility could perhaps be gleaned from the above mentioned Fig. 3.

Although it is important to describe all the observed acoustic phenomena such as the resonances inside the experimental cell qualitatively, for the purposes of quantitative description and comparison with the models, we shall concentrate on the measurements that are most likely unaffected by these extra resonances. In Figs. 7, 8, 9 which show the linewidth of the 77 kHz tuning fork in its can versus temperature and pressure, these data correspond to the (quasi-continuous) floor of the graph, as it is plausible that the peaks in the linewidth correspond to level crossing events. These figures show the comparison of the experimental data with the predictions of the individual models. The small variations of pressure in the temperature dependences (Figs. 7, 8) have been fully taken into account, as well as the small variation of temperature in the pressure dependence data (Fig. 9).

As all the models of acoustic emission contain one constant (denoted $C_{3\mathrm{D}}$, $C_{2\mathrm{D}}$, or $C_{\mathrm{C}}$) as a fitting parameter and one more constant, $\alpha$, (depending on the geometry of the tuning fork in an unknown way) is also included in the viscous drag force, the following procedure was introduced to determine the values of these four constants that would describe all the experiments performed with the same 77 kHz fork

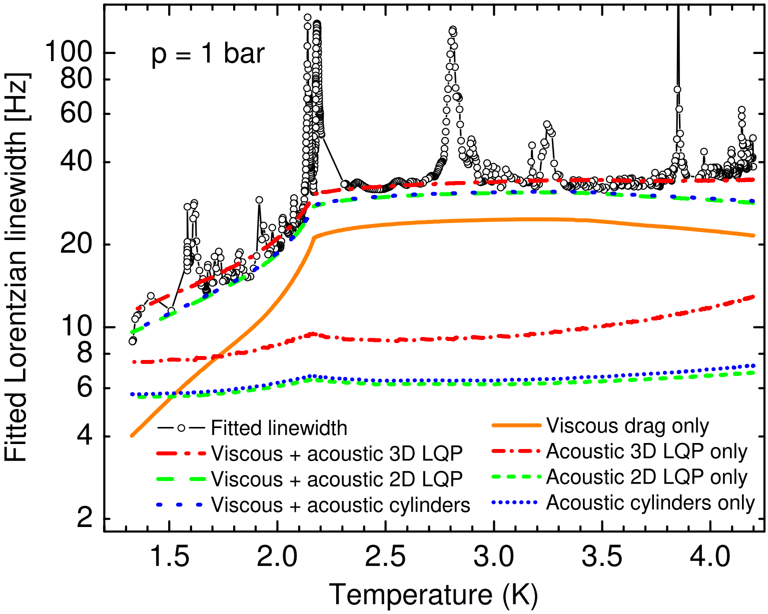

**Fig. 7** (Color online) Temperature dependence of the 77 kHz tuning fork linewidth measured at a fixed pressure of 1 bar—(*black*) *open circles*—is compared to the results of the three models of acoustic emission. For this purpose, the linewidth due to the viscous drag force calculated according to [12] is also added to the dissipation due to acoustic emission as well as displayed separately. The (*red*) *dash-dotted lines* represent the results of the 3D longitudinal quadrupole model, the (*green*) *dashed lines* the 2D quadrupole model, the (*blue*) *dotted lines* the 2D cylinders model each with (*long dots* and *dashes*) and without (*short dots* and *dashes*) the viscous drag added to them. Finally the (*orange*) *solid line* represents the magnitude of the viscous drag alone. It is clearly seen here that at about 1.5 K, the viscous drag is comparable to the losses due to acoustic emission and at lower temperatures, sound emission becomes the dominant dissipative process. Note also the sound resonances/level-crossing events seen as sharp peaks in the experimental data

(i.e., temperature dependence at 1 bar—Fig. 7, temperature dependence at high pressure (24.78–21.36 bar)—Fig. 8, and pressure dependence at about 1.35 K—Fig. 9) as accurately as possible. First, the viscous drag constant, $\alpha$, was estimated from the temperature dependence at high pressure as there the speed of sound reaches its maximum [31, 32] and therefore the acoustic emission power its minimum. Having thus estimated the viscous dissipation, the temperature dependence at 1 bar, and the pressure dependence were then both used to estimate the constants pertaining to the individual models of acoustic emission, $C_{3D}$, $C_{2D}$, $C_C$ for the 3D longitudinal quadrupole, 2D longitudinal quadrupole and 2D cylinders models, respectively. The obtained values of acoustic emission power were then used to refine the viscous dissipation constant by comparison to the high pressure data, and two more iterations like this were performed until the fine details have been settled within the limits of accuracy. The values of the fitting parameters obtained this way follow: $\alpha = 0.59$, $C_{3D} = 15$, $C_{2D} = 4.55$ and $C_C = 1.06$. We see that the 3D model, which was expected to underpredict the emission power requires the highest correction factor to match the experimental data. On the other hand, the cylinders model, which was ex-

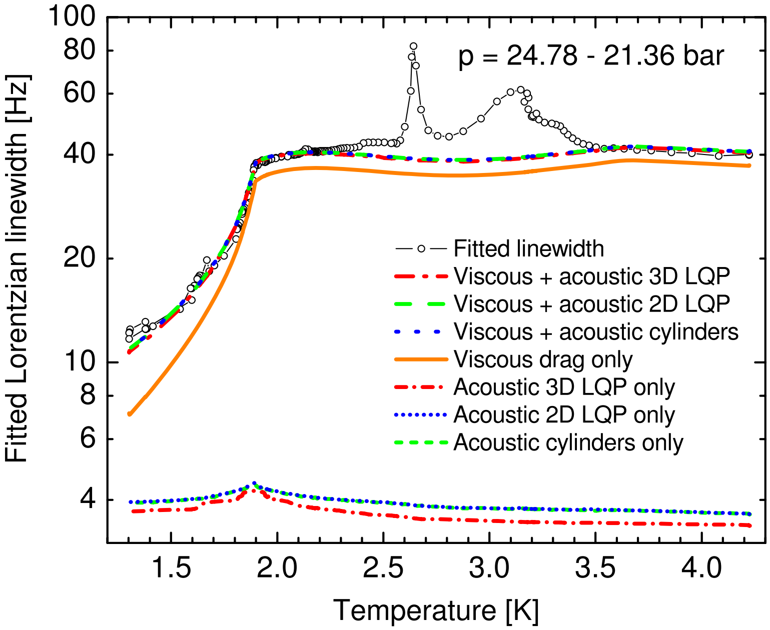

**Fig. 8** (Color online) Temperature dependence of the 77 kHz tuning fork linewidth measured at slightly varying high pressures is compared to the results of the three models of acoustic emission. The symbols, line styles and colors are the same as in Fig. 7. In this case, the drag force is completely dominated by viscosity except for the lowest temperatures. The data are described very well in the whole range except for the vicinity of the cell resonances. Please note the minimum in the expected viscous drag force in the same region—it is present here, because, as was mentioned in the text, we take into account the pressure falling slowly during the experiment, due to additional condensation of helium inside the capillary connected to the cell during cooldown as well as potential small leaks of helium gas from the room temperature part of the pressurizing system. The pressure has been recorded for every experimental point, and in the models, we use an interpolation of these pressures (differing from the actual pressures by less then 1 percent) to calculate the correct dissipation rates corresponding to the actual experimental situation

pected to overpredict the emission power slightly, matches the experiment very well even without this correction factor. However this may be simply due to a numerical coincidence as none of these models accounts for the influence of multiple reflections explicitly, which would in effect lead to another constant correction factor.

Considering the large amount of simplifications present in the models themselves and in the complicated description of the reflection of sound waves at the boundary with the aluminium can, the achieved agreement with the data, using only a single fitting parameter, is rather astonishing. Figures 7–9 also show the relative magnitudes of the viscous and acoustic drag forces and a crossover of their mutual importance is seen clearly, except in the high pressure data set.

## 5 Acoustic Emission by Other Common Oscillatory Structures

Let us give a brief overview of dissipative acoustic properties of other oscillating bodies that have been frequently used as flow generators and detectors in the studies

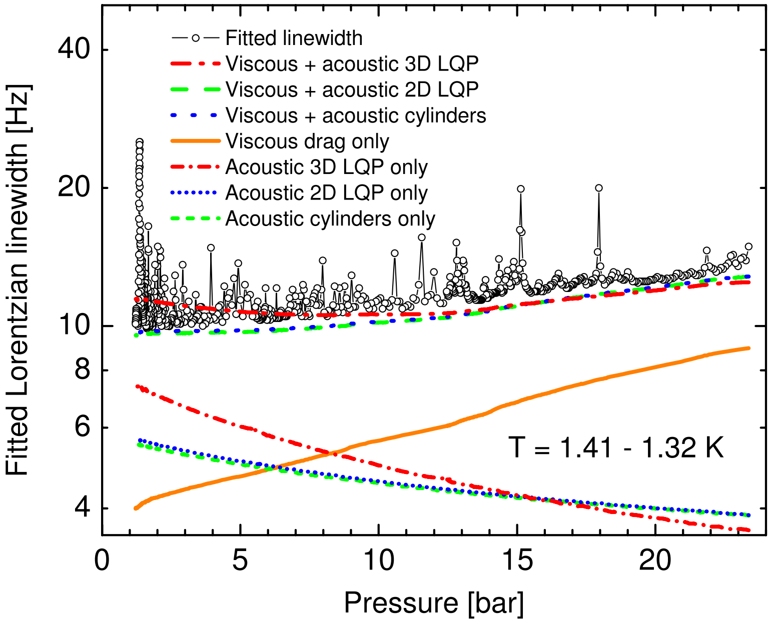

**Fig. 9** (Color online) Pressure dependence of the 77 kHz tuning fork linewidth measured at the lowest temperature of our glass cryostat is compared to the results of the three models of acoustic emission. The symbols, line styles and colors are the same as in Fig. 7. The observed linewidth hardly changes due to the balance of two competing effects. The acoustic drag increases with reduced pressure (and lower speed of sound), however, at the same time, the fraction of the normal component decreases significantly and the viscous drag force is thus reduced. Temperature also kept dropping slightly during the experiment due to helium being released from the pressure cell as well as the overall dropping amount of helium in the cryostat bath, but these changes were taken into account during data processing. This figure also illustrates the small differences between the 3D and 2D models of acoustic emission. The experimental data seem to be described better by the 2D models

of normal or superfluid helium (for a review, see Ref. [34]). These include wires [35–40], spheres [41–44] and grids [45–47]. Our aim is to provide quantitative estimates of the respective emission powers and of the influence of acoustic emission on the overall damping the oscillators experience. However, we restrict ourselves by considering application of vibrating structures in cryogenic $^4$He. Acoustic properties of $^3$He such as zero sound and various sound modes in superfluid $^3$He phases as well as Andreev reflection stay outside the scope of this paper.

None of the objects described below can compare with the high frequency tuning forks described in Sect. 4 in terms of the emission power and we believe that none of them will feel a significant measurable acoustic drag force above 1 K in $^4$He, because it would be *at least* two orders of magnitude lower than the viscous drag force and therefore negligible. However, for some of these oscillators, the situation might be different at lower temperatures where the viscous drag is highly suppressed due to the low fraction of the normal component. Moreover, if the temperature is reduced even further, the hydrodynamic continuum approach is no longer valid and the “laminar” drag force has to be expressed based on the considerations of ballistic propagation of thermal quasiparticles, in which case the drag force is expected to drop with decreasing temperature as $T^4$ [4].

There is a principal difference between tuning forks and other vibrating structures as spheres, wires, grids or micromachined sensors in that these are dipolar acoustic sources and our previous models of acoustic emission are thus not applicable for them. On the other hand, it is possible to calculate dipolar acoustic emission in a similar way as shown in Sect. 3. The following (23) represents both the full calculation and the long-wavelength limit for an acoustic dipole. Additionally, analytical solution for a sphere (24), including the effects of the finite viscous boundary layer, is given in Ref. [21]. Both are listed below, giving the respective emission powers as:

$$P = \frac{B^2 \rho \omega}{4d} \sum_{\substack{m=1 \\ odd}}^{\infty} (2m+1) J^2_{m+1/2}(kd) \approx \frac{B^2 \rho \omega^4 d^2}{6\pi c^3}; \tag{23}$$

$$P = \frac{\pi \rho r^6 \omega^4 U^2}{6c^3} \left( 1 + \frac{3}{\kappa} + \frac{9}{2\kappa^2} + \frac{9}{2\kappa^3} + \frac{9}{4\kappa^4} \right), \tag{24}$$

where $2d$ is the distance between the two point sources comprising the acoustic dipole, $\kappa$ is the ratio of the radius of the sphere to the viscous penetration depth $\delta = \sqrt{2\nu/\omega}$, and all other symbols have the same meaning as in Sect. 3.

### 5.1 Oscillating Spheres

We consider oscillating spheres such as described by Schoepe et al. [41, 43], Luzuriaga [42] and Hemmati et al. [44]. The emission power was calculated using (24) and the laminar drag was either taken from the experimental data, which might also include the intrinsic damping of the oscillator that would have been observed in vacuum, or estimated using the well-known Stokes formula (taking into account the drag of the normal fluid only) modified for oscillatory flows:

$$F = 6\pi \eta_{\mathrm{n}} r U \left( 1 + \frac{r}{\delta} \right), \tag{25}$$

where $\eta_{\mathrm{n}}$ is the dynamic viscosity of $^4$He at 1.2 K [48], $r$ denotes the radius of the sphere, and $U$ stands for the velocity amplitude of the sphere, meaning that $F$ also represents the amplitude of the viscous drag force.

For the spheres used in Refs. [41, 43], the acoustic drag was found to be at least 9 orders of magnitude below the laminar drag at 1.2 K; for spheres used by Schoepe et al., this ratio is valid even when compared to the linear drag as measured at 300 mK. For the sphere used by Luzuriaga [42], the ratio was not so huge—acoustic emission was found about four to five orders of magnitude lower than the viscous drag at 1.2 K. It is therefore safe to conclude that for all practical purposes, acoustic emission can indeed be neglected. This holds as well for the niobium sphere used in Ref. [44].

### 5.2 Vibrating Wire Resonators

For the vibrating wire resonators, we estimate acoustic emission in two different ways. First, we consider the wire as an acoustic dipole consisting of two point sources in 3D fluid and second, we replace it by a model sphere of the same surface area. The acoustic dipole approach can be justified by the fact that at typical resonance frequencies (≈1 kHz), the size of the wire (usually about 3 mm) is much smaller than the wavelength of sound waves in $^4$He, which is of order 20 cm. This approach, however, neglects the effects of the viscous boundary layer completely, we therefore additionally use the model of a replacement sphere to estimate its magnitude. We define the acoustic source strength $B = A\,U_{\mathrm{eff}}$, where $A$ is the projected area of the wire on the plane perpendicular to its motion, and $U_{\mathrm{eff}}$ is an estimate of the effective velocity along the wire, which we define arbitrarily as $U_{\mathrm{eff}} \approx 0.3\,U$ for the purposes of these order of magnitude estimates. The separation of the two point sources is assumed to be equal to the diameter of the wire.

In some cases the vibrating wire would perhaps be better represented as a long oscillating cylinder with a finite viscous penetration depth. However, we do not discuss such calculations here, as the magnitude of acoustic damping appears to be extremely low for typical vibrating wire resonators (such as described in Refs. [35–40]) and the extra precision in the estimate of emission power would therefore be of little importance. Again, for all the cases considered, the acoustic emission was found very low, about 9 orders of magnitude below the laminar drag force at 1.2 K and therefore negligible for all practical purposes.

### 5.3 Oscillating Grids

We consider here the case of the Lancaster circular grid of 8 cm diameter driven electrostatically at its resonance frequency about 1 kHz as described in Refs. [45–47]. The emission power was estimated using the acoustic dipole model, where the source strength B was taken as $B = A\,U_{\mathrm{eff}}$, where $A$ is the total projected area of the wires (determined as the area of the grid multiplied by $(1-\tau)$, where $\tau$ is transparency of the grid) and $U_{\mathrm{eff}}$ is an effective velocity, $U_{\mathrm{eff}} = 0.432\,U$, that takes into account the profile of the fundamental flexural resonance mode of the grid [47] in a form of a zero order Bessel function. We assume the separation of the sources to be equal to the thickness of the grid (6 μm).

When the linewidth due to acoustic emission is compared to the experimental linewidth measured at the base temperature of a dilution refrigerator (about 10 mK), which is very similar to its vacuum value, we find that the acoustic emission contribution is roughly three orders of magnitude lower than this experimentally observed damping. However, in the measured damping, the dominant contribution is the nuisance damping due to the grid material, therefore a direct comparison with viscous/ballistic drag forces is not possible. When separated from the nuisance damping, these losses might in principle turn out to be comparable with the acoustic drag at this very low temperature and, moreover, dispersive effects of sound emission might be observable as well. Still, we believe that it would be an experimental challenge to detect acoustic emission using the vibrating grid of the described geometry.

### 5.4 Micromachined Devices

Lately, significant effort has been invested in developing very small and highly sensitive vibrating sensors for cryogenic fluid dynamics using technologies such as electron beam lithography and selective etching. With these, it is possible to fabricate oscillators of micron (MEMS) and recently even submicron (NEMS) sizes. As a representative of these sensors, we consider a $7 \times 3\ \mu\text{m}^2$ goal-post shaped oscillator of beam cross-section $220 \times 100\ \text{nm}^2$ resonating at 7.1 MHz developed in Grenoble and described by Collin et al. [49].

Even at this high frequency, the oscillator is still smaller than the wavelength of about 30 μm, which justifies the application of the 3D dipole source model to estimate its acoustic emission power. From similar considerations as above, where the 7 μm "paddle" is considered perfectly solid and the two 3 μm "legs" as ideal Euler cantilevers, it follows that the acoustic drag in liquid $^4$He at 1.2 K is almost three orders of magnitude lower than the viscous drag and therefore does not represent any serious influence on the behavior of the oscillator, unless the temperature is reduced well below 1 K—here a possible influence might be observable depending on the exact geometry and other experimental conditions, especially the nuisance damping. Again, dispersive effects may in principle be seen as well.

### 5.5 Standard 32 kHz Tuning Forks

In this work we deliberately used high frequency forks in order to make this experimental study feasible. We have already shown that a crossover of the viscous and acoustic drag forces may occur for these forks at temperatures as high as 1.5–2 K. This effectively disqualifies the high frequency tuning forks from use as sensors at very low temperatures below 1 K, as other relevant damping mechanisms (viscous/ballistic/intrinsic drag) will most likely be screened by acoustic emission. It is then natural to raise the question whether a similar phenomenon will take place with the standard 32 kHz tuning forks and at which temperature it might be expected to occur in $^4$He.

To tackle this problem, we will apply the infinite cylinders model that describes our experimental data obtained with the 77 kHz fork perhaps most accurately. When applied to the 32 kHz forks, it seems that at about 1 K the acoustic drag might be comparable in order of magnitude with the viscous/ballistic dissipation, therefore the final balance of these dissipative mechanisms depends on finer details relevant for acoustic emission, such as the geometry of both the tuning fork and the experiment and the reflectivity of the boundaries. We therefore provide estimates for several types of tuning forks. The forks from Table 1 are complemented by two other types of 32 kHz forks—F32a (large fork) and F32c (small fork)—referred to in [12] as A1 and C3, respectively. For each fork, we list two values of the ratio of acoustic to viscous drag: (i) assuming no reflections at all, and (ii) assuming an overall 99% reflectivity of the container walls. These ought to serve as illustrative examples giving approximate upper and lower bounds for the expected acoustic emission power in comparison to the losses due to viscous drag. We neglect acoustic resonances due to the cell geometry as well as all dispersive effects as well as dissipative processes that are responsible for damping the propagating sound waves inside the liquid helium. The explicit ratios of acoustic to viscous drag force are summarized in Table 2, including the corresponding values for 77 kHz and 100 kHz tuning forks for comparison. To understand Table 2 correctly, we should realize that in practical experiments (maybe except for very large volumes of helium) some finite amount of reflection on the walls will always occur, reducing the resulting emission power and shifting the ratio toward the

**Table 2** Estimated ratios of acoustic to viscous drag acting on 32 kHz tuning forks in liquid $^4$He at 1.2 K and saturated vapor pressure. For experimental conditions where strong reflection on solid boundaries can be expected, such as presented in Sect. 4, one should refer to the values listed in the second column. See the accompanying text for details

| Fork type | Acoustic to viscous drag ratio | |
|---|---|---|
| | no reflection | 99% reflectivity |
| F32 | 22 | 0.22 |
| F32s | 0.20 | 0.0020 |
| F32a | 8.9 | 0.089 |
| F32c | 0.21 | 0.0021 |
| F38 | 58 | 0.58 |
| F77 | 310 | 3.1 |
| F100 | 2700 | 27 |

value calculated for 99% reflectivity (which more or less corresponds to the situation when the tuning fork is enclosed inside its original can). It therefore follows that in this situation even the large 32 kHz forks will not show strong effects due to acoustic emission at 1.2 K, however, at the same time it is obvious that the ratios of acoustic to viscous drag will change dramatically with the temperature falling below 1 K.

This calculation together with the general formulae given in Sect. 3 shows that it is advisable to use smaller types of tuning forks for sensitive low temperature experiments as they generally display lower losses due to acoustic emission. In order to suppress their acoustic emission even further, we could recommend enclosing them in a sufficiently small experimental volume with highly reflecting walls to minimize the radiation losses as well as the possibility of coupling to acoustic resonances of the cell.

## 6 Conclusions

We have used a set of quartz tuning forks oscillating at 32, 38, 77 and 100 kHz in experiments aiming to clarify the role of acoustic emission in the overall dissipation experienced by these structures oscillating in cryogenic gaseous and liquid $^4$He. Thanks to the very steep frequency dependence of the emission power, the high frequency (77 and 100 kHz) forks allowed reliable measurement of acoustic emission even above 1.2 K in a pressure cell placed inside an ordinary helium bath glass cryostat and gave conclusive quantitative evidence of this phenomenon. Level crossing events have been observed both in gaseous and liquid $^4$He and associated with acoustic resonances due to the geometry of the experimental cell. Additionally, complementary experiments with all the forks have been performed at 350 mK in a dilution refrigerator and provided direct evidence of the acoustic emission and its frequency scaling in the temperature range corresponding to the ballistic drag regime in superfluid $^4$He.

We have considered three models of acoustic emission by tuning forks—3D quadrupole emission, 2D quadrupole emission and the emission by two infinite transversely oscillating cylinders (also 2D). We have calculated the expected emission powers and compared them with the experimental data taking into account also the acoustic properties of the boundaries delimiting the fluid volume. While all the models gave reasonable agreement with the pressure and temperature dependences obtained experimentally using the 77 kHz fork, the data are best described by the 2D models, which behave almost identically in the studied range except for the values of their multiplicative parameters. The infinite cylinders model supplemented with the considerations of reflection on the boundaries fits the data obtained in a wide parameter space ($1.3\ \text{K} < T < 4.2\ \text{K}$, $0 < p < 25$ bar) with the precision of about 6% even without any fitting parameter, although this might be due to a numerical coincidence. Nevertheless, these results give us confidence that the same models can be used to predict the significance of acoustic emission for the commonly used 32 kHz forks. Moreover, a similar approach modified for dipole emission has been used to estimate the emission powers of other oscillating structures, such as spheres, wires, grids, MEMS and NEMS, used by others and described in literature.

We hope that these measurements, the proposed models, and the discussion in Sect. 5 will serve other investigators working with tuning forks and other oscillators in liquid helium and provide them with an estimate of the relative importance of acoustic emission in their experiments.

**Acknowledgements** We are grateful to A. Salmela, S. Babuin, D. Garg, P.V.E. McClintock and W.F. Vinen for stimulating discussions. We also acknowledge the thorough work of all the reviewers who raised a number of useful questions, suggestions and comments that led us to clarify some of the issues under discussion. This research was supported by research plans MS 0021620834 and by GAČR 202/08/0276.

## References

1. E.P. Eernisse, R.W. Ward, R.B. Wiggins, IEEE Trans. Ultrason. Ferroelectr. Freq. Control **35**, 3230 (1988)
2. K. Karrai, R.D. Grober, Tip-sample distance control for near-field scanning optical microscopes, in *Near-Field Optics*, ed. by M.A. Paesler, P.T. Moyer. Proc. SPIE, vol. 2535 (1995), p. 69
3. M. Blažková, M. Človečko, V.B. Eltsov, E. Gažo, R. de Graaf, J.J. Hosio, M. Krusius, D. Schmoranzer, W. Schoepe, L. Skrbek, P. Skyba, R.E. Solntsev, W.F. Vinen, J. Low Temp. Phys. **150**, 525 (2008)
4. R. Blaauwgeers, M. Blažková, M. Človečko, V.B. Eltsov, R. de Graaf, J. Hosio, M. Krusius, D. Schmoranzer, W. Schoepe, L. Skrbek, P. Skyba, R.E. Solntsev, D.E. Zmeev, J. Low Temp. Phys. **146**, 537 (2007)
5. P. Skyba, J. Low Temp. Phys. **160**, 219 (2010)
6. E.M. Pentti, J.T. Tuoriniemi, A.J. Salmela, A.P. Sebedash, J. Low Temp. Phys. **150**, 555 (2008)
7. L. Skrbek, M. Blažková, T.V. Chagovets, M. Rotter, D. Schmoranzer, J. Low Temp. Phys. **150**, 194 (2008)
8. M. Blažková, D. Schmoranzer, L. Skrbek, J. Low Temp. Phys. **34**, 380 (2008)
9. E.M. Pentti, J.T. Tuoriniemi, A.J. Salmela, A.P. Sebedash, Phys. Rev. B **78**, 064509 (2008)
10. M. Blazkova, D. Schmoranzer, L. Skrbek, Phys. Rev. E **75**, 025302 (2007)
11. D. Schmoranzer, M. Král'ová, V. Pilcová, W.F. Vinen, L. Skrbek, Phys. Rev. E **81**, 066316 (2010)
12. M. Blažková, D. Schmoranzer, L. Skrbek, W.F. Vinen, Phys. Rev. B **79**, 054522 (2009)
13. G. Sheshin, A.A. Zadorozhko, E. Rudavskii, V. Chagovets, L. Skrbek, M. Blazhkova, J. Low Temp. Phys. **34**, 875 (2008)
14. M. Blažková, M. Človečko, E. Gažo, L. Skrbek, P. Skyba, J. Low Temp. Phys. **146**, 305 (2007)
15. D.I. Bradley, M.J. Fear, S.N. Fisher, A.M. Guénault, R.P. Haley, C.R. Lawson, P.V.E. McClintock, G.R. Pickett, R. Schanen, V. Tsepelin, L.A. Wheatland, J. Low Temp. Phys. **156**, 116 (2009)
16. D.I. Bradley, M. Človečko, E. Gažo, P. Skyba, J. Low Temp. Phys. **152**, 147 (2008)
17. D.I. Bradley, P. Crookston, S.N. Fisher, A. Ganshin, A.M. Guénault, R.P. Haley, M.J. Jackson, G.R. Pickett, R. Schanen, V. Tsepelin, J. Low Temp. Phys. **157**, 476 (2009)

18. D. Schmoranzer, L. Skrbek, J. Phys. Conf. Ser. **150**, 012048 (2009)
19. D.O. Clubb, O.V.L. Buu, R.M. Bowley, R. Nyman, J.R. Owers-Bradley, J. Low Temp. Phys. **136**, 1 (2004)
20. D. Garg, V.B. Efimov, M. Giltrow, P.V.E. McClintock, L. Skrbek, W.F. Vinen, Mutual interactions between oscillating objects in superfluid $^4$He: critical velocities and the persistence of remanent vortices, Europhys. Lett. (submitted)
21. L.D. Landau, E.M. Lifshitz, *Hydrodynamics*, 2nd edn. (Pergamon Press, New York, 1987)
22. C.L. Morfey, M.C.M. Wright, Proc. R. Soc. Lond. Ser. A, Math. Phys. Sci. **463**, 2101–2127 (2007)
23. K.M. Li, S. Taherzadeh, K. Attenborough, J. Acoust. Soc. Am. **101**, 3343–3352 (1997)
24. K.M. Li, S. Taherzadeh, J. Acoust. Soc. Am. **102**, 2050–2057 (1997)
25. R.M. Sillitto, Am. J. Phys. **34**, 639 (1966)
26. D.A. Russell, Am. J. Phys. **68**, 1139 (2000)
27. I.M. Khalatnikov, *Theory of Superfluidity* (Nauka, Moscow, 1971) (in Russian)
28. S.P. Timoshenko, D.H. Young, *Theory of Structures*, 2nd edn. (McGraw-Hill College, New York, 1965)
29. M. Abramovitz, I.A. Stegun, *Handbook of Mathematical Functions*. Applied Mathematics Series, vol. 55 (National Bureau of Standards, Washington, 1964)
30. P.M. Morse, K.U. Ingard, *Theoretical Acoustics* (Princeton University Press, Princeton, 1986)
31. R.D. McCarty, Thermophysical properties of Helium-4 from 2 to 1500 K with pressures to 1000 atmospheres, Technical Note 631 National Bureau of Standards (1972)
32. V.D. Arp, R.D. McCarty, The properties of critical helium gas, Tech. Rep., U. of Oregon (1998)
33. G.L. Pollack, Rev. Mod. Phys. **41**, 48 (1969)
34. L. Skrbek, W.F. Vinen, The use of vibrating structures in the study of quantum turbulence, in *Progress in Low Temperature Physics*, ed. by M. Tsubota, W.P. Halperin, vol. XVI (Elsevier, Amsterdam, 2009), Chap. 4
35. M. Morishita, T. Kuroda, A. Sawada, T. Satoh, J. Low Temp. Phys. **76**, 387 (1989)
36. H. Yano, A. Handa, H. Nakagawa, K. Obara, O. Ishikawa, T. Hara, M. Nakagawa, J. Low Temp. Phys. **138**, 561 (2005)
37. H. Yano, N. Hashimoto, A. Handa, M. Nakagawa, K. Obara, O. Ishikawa, T. Hata, Phys. Rev. B **75**, 012502 (2007)
38. R. Goto, S. Fujiyama, H. Yano, Y. Nago, N. Hashimoto, K. Obara, O. Ishikawa, M. Tsubota, T. Hata, Phys. Rev. Lett. **100**, 045301 (2008)
39. H. Yano, T. Ogawa, A. Mori, Y. Miura, Y. Nago, K. Obara, O. Ishikawa, T. Hata, J. Low Temp. Phys. **156**, 132 (2009)
40. D.I. Bradley, S.N. Fisher, A.M. Guénault, R.P. Haley, V. Tsepelin, G.R. Pickett, K.L. Zaki, J. Low Temp. Phys. **154**, 97 (2009)
41. J. Jäger, B. Schuderer, W. Schoepe, Phys. Rev. Lett. **74**, 566 (1995)
42. J. Luzuriaga, J. Low Temp. Phys. **138**, 267 (1997)
43. M. Niemetz, H. Kerscher, W. Schoepe, J. Low Temp. Phys. **126**, 287 (2002)
44. A.M. Hemmati, S. Fuzier, E. Bosque, S.W. VanSciver, J. Low Temp. Phys. **156**, 71 (2009)
45. H.A. Nichol, L. Skrbek, P.C. Hendry, P.V.E. McClintock, Phys. Rev. Lett. **92**, 244501 (2004)
46. H.A. Nichol, L. Skrbek, P.C. Hendry, P.V.E. McClintock, Phys. Rev. E **70**, 056307 (2004)
47. D. Charalambous, L. Skrbek, P.C. Hendry, P.V.E. McClintock, W.F. Vinen, Phys. Rev. E **74**, 036307 (2006)
48. R.J. Donnelly, C.F. Barenghi, J. Phys. Chem. Ref. Data **27**, 1217 (1998)
49. E. Collin, T. Moutonet, J.S. Heron, O. Bourgeois, Yu.M. Bunkov, H. Godfrin, A tunable hybrid electro-magnetomotive NEMS device for low temperature physics. J. Low Temp. Phys. **162**, 653 (2011)